ARTICLE:

"THERMAL-INFRARED SPECTRAL AND ANGULAR CHARACTERIZATION OF CRUDE OIL AND SEAWATER EMISSIVITIES FOR OIL SLICK IDENTIFICATION"

AUTHORS: Raquel Niclòs, Carolina Doña, Enric Valor and Mar Bisquert

AFFILIATION: Earth Physics and Thermodynamics Department, University of Valencia, 50 Dr. Moliner, E-46100 Burjassot, Valencia, Spain.

CONTACT INFORMATION:

Corresponding author: Dr. Raquel Niclòs

Address: 50 Dr. Moliner, E-46100 Burjassot, Valencia, Spain.

E-mail: Raquel.Niclos@uv.es

Phone: +34 963543308

Fax: +34 963543385

ABSTRACT

Previous work has shown that crude oil emissivity is lower than that of seawater in the thermal-infrared (TIR) spectrum. Thus, oil slicks cause an emissivity decrease relative to seawater in that region. The aim of this paper was to carry out experimental measurements to characterize crude oil and seawater emissivity spectral and angular variations. The results showed that crude oil emissivity is lower than seawater emissivity and essentially flat in the 8 - 13 μm atmospheric window. Crude oil emissivity has a marked emissivity decrease with angle (from 0.956±0.005 at 15º to 0.873±0.007 at 65º), even higher than that of seawater, and thus the seawater-crude emissivity difference increases with angle (from +0.030±0.007 at close-to-nadir angles up to +0.068±0.010 in average at 65º).

In addition, the experimental results were checked by using the dual-angle viewing capability of the ENVISAT-AATSR images (i.e., 0º-22º and 53º-55º for nadir and forward views respectively), with data acquired during the BP Deepwater Horizon oil slick in 2010. The objective was to explore the applicability to satellite observations. Nadir-forward emissivity differences of +0.028 and +0.017 were obtained for the oil slick and surrounding clean seawater respectively. Emissivity differences between the seawater and oil slick were +0.035 and +0.046 for nadir and forward views respectively, in agreement with the experimental data.

The increase of seawater-crude emissivity difference with angle gives significant differences for off-nadir observation angles, showing a new chance of crude oil slick identification from satellite TIR data.

Keywords: Emissivity, Thermal-Infrared, Crude Oil, Seawater, Oil Slick, Angular Variation.

1. INTRODUCTION

When freight ships, carrying tens of thousands of tons of crude oil or fuel, crash, malfunction, or encounter harsh weather, they may spill part of their loads into seawater. The quantity of oil spilled during ship, oilrig and pipeline accidents has ranged from a few hundred tons to several tens or even hundreds of thousand tons (www.itopf.com). E.g., the Prestige tanker spilled 63,000 tons off the coast of Galicia, Spain, in 2002 [1] and the BP Deepwater Horizon oilrig accident was estimated to have spilled 680,000 tons in the Gulf of Mexico in 2010 [2]. The oil spreads out into a layer that hovers on top of the ocean. Oil floats on oceans and seas, covering areas of their surface with a thick film of crude oil; films thicker than 200μm are termed as slicks in [1]. The slicks are difficult to control or contain, and even more challenging to clean up. For environmental applications, early detection of anthropogenic oil slicks can make possible timely protection of critical habitats and help identify polluters [3]-[4]. Thus, the detection of oil slicks is an important environmental objective to which remote sensing techniques can contribute. The development of remote sensing techniques for oil slick detection has used spectral information from ultraviolet to microwave wavelengths [1], [3]. Oil fluoresces in the ultraviolet but the intensity and the atmospheric transmission is poor in this region, making satellite observation difficult [3], [5]. An airborne ultraviolet laser can illuminate the ocean exciting petroleum components in an oil slick, having different fluorescence spectra for different oil types [6]. In this region, water column or organic material can interfere with oil signature for thin oil films. In the visible and infrared region the spectral reflectance properties vary with oil type, emulsion level and film thickness [4], [7], and crude detection is complex because surface roughness changes water reflectance, making the reflectance contrast between seawater and crude oil dependent on the sea surface state and the viewing geometry [3], [8]. In both the Thermal-Infrared (TIR) and microwave regions, crude oil and seawater have different emissivity values [1], [3]-[4], [9]-[10] resulting in a contrast that can be

used for oil slicks detection. The smoothing effect of oil on water also can be detected by radar [1], [11]-[13], but many other factors can cause sea surface smoothing, providing false targets.

This paper explores TIR responses of crude oil and seawater and how their spectral and angular behaviors could contribute to improve the detection of crude oil slicks from TIR satellite images. Previous papers [3]-[4] measured crude oil spectral emissive responses in the 8-13μm region. We additionally characterize here the angular dependences of crude oil and seawater by using angular measurements carried out by multichannel radiometers in that spectral region. Section 2 describes the experimental methodology and strategy used for the measurements. Section 3 shows the spectral and angular emissivity variations obtained from the experimental data. Section 4 checks the experimental results by using satellite TIR data, and finally Section 5 summarizes the main conclusions of the study.

2. MEASUREMENT METHODOLOGY AND STRATEGY

2.1. Experimental samples

Crude oil and seawater samples were alternatively measured during the experiment. The crude oil was provided by Repsol S.A., which also provided sample chemical and physical analyses in the framework of a collaboration agreement between the University of Valencia and Repsol. The crude oil sample properties are summarized in Table I. It was relatively light oil (i.e., high ºAPI, low viscosity, high percentage of saturated hydrocarbons) with a tendency to paraffinic. The seawater was collected from the Mediterranean Sea, with a salinity of 34 psu.

2.2. Instrumentation

TIR measurements were made with two Cimel Electronique CE312 radiometers with six bands placed within 8 – 13 μm [14] (www.cimel.fr): 8-13, 8.1-8.5, 8.5-8.9, 8.9-9.3, 10.3-11.0, and

11.0-11.7 μm, with effective wavelengths of 10.5, 8.4, 8.7, 9.1, 10.6 and 11.3 μm, respectively. The instruments were calibrated against a LANDCAL P80P blackbody source (www.ametek-land.com) for temperatures from 5 to 35 °C before the experiment. Linear calibration equations were established for the radiometer bands, with estimated errors less than ± 0.03 K in terms of brightness temperature for all bands, although the radiometer accuracy was ± 0.1 K according to the manufacturer (www.cimel.fr). The CE312 radiometers participated in a comparison of infrared instruments organized by the Committee on Earth Observation Satellites (CEOS) against reference, traceable instruments [15]. Results showed that the CE312 radiometers agreed with the reference blackbody within a maximum uncertainty of ±0.2 K for all bands at 20–30 °C.

NTC thermistors were used to measure the thermodynamic surface temperature required to retrieve emissivities from TIR radiance measurements (see section 2.3). They were located just below the sample surfaces. The thermistors were calibrated previously using a thermal bath and a high-accuracy platinum probe as a reference. The thermistor uncertainties after the calibration were lower than ± 0.1 K.

Additionally, a TESTO 880 TIR camera (www.testo.es), with a sensitivity of ± 0.1 K, was used to check the spatial thermal homogeneity of samples.

2.3. Methodology

The radiance measured by the band *i* of a TIR radiometer observing a surface at ground level at a direction (θ,ϕ) can be expressed as follows:

$$L_i(\theta,\phi) = \varepsilon_i(\theta,\phi)B_i(T) + L_i^{ref}(\theta,\phi) \quad (1)$$

where $B_i(T)$ is the averaged Planck's function for the band *i* and a temperature *T*; $\varepsilon_i(\theta,\phi)$ is the directional surface emissivity; and $L_i^{ref}(\theta,\phi)$ is the reflection of the downwelling sky radiance on the surface, which is given by the equation:

$$L_i^{ref}(\theta,\phi) = \frac{1}{\pi}\int_0^{2\pi}\int_0^{\pi/2} f_{b,i}(\theta',\phi',\theta,\phi) L_i^{\downarrow}{}_{atm}(\theta',\phi')\cos\theta'\sin\theta' d\theta' d\phi' \quad (2)$$

where $L_i^{\downarrow}{}_{atm}(\theta',\phi')$ is the incident sky radiance in the direction (θ',ϕ'), and $f_{b,i}(\theta',\phi',\theta,\phi)$ is the bidirectional reflectance distribution function (BRDF), which is related with the directional emissivity by using the following expression [16]-[17]:

$$\varepsilon_i(\theta,\phi) = 1 - \int_0^{2\pi}\int_0^{\pi/2} f_{b,i}(\theta',\phi',\theta,\phi)\cos\theta'\sin\theta' d\theta' d\phi' \quad (3)$$

When a specular reflection can be considered, e.g. for water surfaces [18], the reflection term can be rewritten:

$$L_i^{ref}(\theta,\phi) = \left[1-\varepsilon_i(\theta,\phi)\right] L_i^{\downarrow}{}_{atm}(\theta,\phi\pm\pi) \quad (4)$$

If the thermodynamic or kinetic surface temperature T is known, equations (1) to (4) allow the recovery of $\varepsilon_i(\theta,\phi)$ from radiometric measurements of $L_i(\theta,\phi)$ and $L_i^{\downarrow}{}_{atm}(\theta,\phi\pm\pi)$ as follows [19]:

$$\varepsilon_i(\theta,\phi) = \frac{L_i(\theta,\phi) - L_i^{\downarrow}{}_{atm}(\theta,\phi\pm\pi)}{B_i(T) - L_i^{\downarrow}{}_{atm}(\theta,\phi\pm\pi)} \quad (5)$$

2.4. Measurement strategy

Measurements of surface and sky radiances ($L_i(\theta,\phi)$ and $L_i^{\downarrow}{}_{atm}(\theta,\phi\pm\pi)$ in (5), respectively) were carried out with the six-band CE312 radiometers mounted on a tripod provided with a goniometer and an inclinometer with an accuracy of ± 0.01º. Zenith angles, θ, of 15º, 30º, 45º, 50º, 55º, 60º, and 65º to nadir were used for the angular measurements. The minimum angle of 15º was established to avoid a possible mirror effect of the radiometer on the sample surfaces. Each set of angular measurements took about 10-12 minutes and consisted of seven surface radiance

measurements, one for each angle, using the six radiometer bands, alternately with seven sky observations for the same angles to zenith. Two extra sky measurements were taken at 0º to zenith and over a LABSPHERE® IRT-94-100 INFRAGOLD TIR diffuse reflectance panel (www.labsphere.com, [20]). This panel allows obtaining the hemispheric downwelling radiance, $L_i^{\downarrow}{}_{atm,hem}$ (i.e., the downwelling irradiance divided by π), by measuring the reflected radiance of the panel from any viewing direction:

$$L_i^{\downarrow}{}_{atm,hem} = \frac{1}{\pi}\int_0^{2\pi}\int_0^{\pi/2} L_i^{\downarrow}{}_{atm}(\theta',\phi')\cos\theta'\sin\theta' d\theta' d\phi' \tag{6}$$

Additionally, the NTC thermistors collected data every half a minute to obtain the concurrent sample temperature used to assess $B_i(T)$ in (5).

A set of angular measurements was first carried out over the seawater sample and then over the crude oil sample and repeated alternatively (a minimum of six times).

The angular sets were carried out on a terrace at the top of the Physics Faculty located in the University of Valencia campus in Burjassot, Spain (the terrace was 4 m higher than the surrounding buildings, the contribution of the surrounding buildings being negligible [20]; 39º 30’ 25’’ N, 0º 18’ 15’’ W). The location assured minimal presence of surrounding elements and measurements were made with cloud-free and low-windspeed conditions at nighttime to avoid sample temperature variations during the measurement process and significant spatial thermal gradients in samples that could affect the contact temperature measurements. The sky radiances measured at the different angles and with the diffuse reflectance panel were used to assure the cloud-free condition of the atmosphere during the measurements. In the case of cloud-free conditions, the sky radiances follow the expressions [21]-[22]:

$$L_i^{\downarrow}{}_{atm}(\theta,\phi) = L_i^{\downarrow}{}_{atm}(\theta) \approx L_i^{\downarrow}{}_{atm}(0^o)\cos^{-x_i}(\theta) \tag{7}$$

$$L_i^{\downarrow}{}_{atm,hem} = \frac{2}{2 - x_i} L_i^{\downarrow}{}_{atm}\ (0^o) \tag{8}$$

These equations were followed during the experiment, as it is shown, e.g., in Fig. 1 by the linear correlation between $\ln(L_i^{\downarrow}{}_{atm}(\theta))$ and $\ln(\cos(\theta))$ described by (7), proving that cloud-free condition were maintained during all the measurements.

The spatial thermal homogeneity of seawater and crude oil samples was checked with the TESTO TIR camera; spatial standard deviations of ±0.2K were obtained in terms of brightness temperatures for the samples.

3. EXPERIMENTAL RESULTS

3.1. Spectral variation

Fig. 2 shows the crude oil and seawater emissivity spectral values measured at the close-to-nadir angle of 15º by using the five narrow spectral bands of the CE312 radiometers and the methodology described in Section 2. Emissivity-axis error bars show measurement uncertainties and wavelength-axis bars show the radiometer spectral band widths. The measurement uncertainties are the largest between the emissivity measurement dispersions and those obtained with the propagation of variable uncertainties in equation (5). The uncertainties described in section 2.2 for the CE312 radiometers and thermistors were considered in this error analysis.

Fig. 2 shows that crude oil emissivity is lower than that of seawater, a feature also reported on earlier papers [3]-[4]. Seawater emissivity spectral values agree with those shown in previous papers for close-to-nadir observation angles [19], [23]-[25] (see Fig. 2). Crude oil results also agree with those in [3] and [4]. Salisbury et al. [3] measured 8-13 μm crude oil reflectances within 4.0-4.5% (i.e., emissivities of 0.955-0.960) for five crude oils with very different compositions and

physical properties, showing little differences between them throughout the spectral range. Lammoglia and De Souza Filho [4] obtained 8-13 μm emissivities from 0.94 to 0.97 also for a variety of samples. Fig. 2 shows similar values for the five CE312 spectral bands (with a mean value of 0.956 and a standard deviation of ±0.001, better than the emissivity measurement error of ±0.005), with a featureless grey-body spectrum within the atmospheric window between 8 and 12 μm, at least at the spectral resolution of the CE312 radiometer. This fact is also in agreement with the results in [3] and [4], which showed similar 8-13 μm emissivity spectral values for a wide variety of crude oil types and slick thicknesses, and pointed out the inability to discriminate different crude oil types quantitatively by using thermal bands positioned in that spectral window, especially from the current satellite sensors due to the coarse spectral resolution in the TIR. This is even in the case of the Earth Observation System (EOS) Terra Advanced Spaceborne Thermal Emission Reflection Radiometer (ASTER) 5-bands thermal spectral resolution.

3.2. Angular variation

Fig. 3 shows again the spectral signature of the crude oil and seawater samples but measured at two angles: 15º and 65º. The spectral signatures measured at 65º are similar to those at 15º, with a slightly higher spectral deviation (a standard deviation of ±0.006 at 65º for the CE312 bands). However, both seawater and crude oil values are lower at 65º than at 15º; the difference between seawater and crude oil emissivities being larger at 65º than at 15º. Angular seawater measurements and models have been published [19], [24]-[29]); the angular variation of seawater emissivity being well-known. However, this is not the case for crude oil slicks.

Fig. 4 shows the seawater and crude oil emissivities measured at θ of 15º, 30º, 45º, 50º, 55º, 60º, and 65º by the six CE312 spectral bands, together with the difference between both samples. The uncertainty associated to the difference is the quadratic sum of seawater and crude oil emissivity uncertainties. Both seawater and crude oil emissivities decrease gradually with angle for

all the spectral bands (with mean differences between 15º and 65º of +0.040±0.009 and +0.078±0.008 for the seawater and crude oil samples, respectively). Crude oil emissivity decreases with angle faster than that of seawater and thus the difference between seawater and crude oil emissivities is larger for off-nadir observation angles, - i.e., greater contrast. Close to nadir, i.e., at 15º, the difference between seawater and crude oil emissivities is +0.030±0.007, which is almost an order of magnitude larger than the emissivity measurement uncertainty. The seawater and crude oil emissivity difference increases with angle up to +0.068±0.010 at 65º on average for all the CE312 bands, with a maximum difference of +0.074±0.010 for the 11.0-11.7 μm band and a minimum of +0.062±0.009 for the 8.5-8.9 μm and 8.9-9.3 μm bands. The significant seawater-crude emissivity difference for off-nadir angles makes oil slick identification more feasible at these angles.

4. SATELLITE IMAGE CROSS-CHECK

The ENVISAT-Advanced Along-Track Scanning Radiometer (AATSR) data were compared with the experimentally measured seawater and crude oil emissivities, their decrease with angle, and the seawater-crude emissivity differences, to explore the applicability to satellite observations. ENVISAT-AATSR had a circular scan pattern, and obtained forward-view measurements at a zenith angle of 53°-55°. Around 100 seconds later, the same region was sampled at a nadir viewing zenith angle of 0°-22°. These near-simultaneous views provide an excellent opportunity for analyzing angular emission variations over homogeneous surfaces like seas, since the different ground instantaneous field of views at the nadir and forward views cause additional differences over heterogeneous surfaces. The future first Sentinel 3 Earth Observation satellite, expected to launch in 2014, will house the Sea and Land Surface Temperature Radiometer (SLSTR), which will be the successor to the decommissioned AATSR and thus will continue with the dual-view capability.

The radiance measured by the band *i* of a satellite TIR radiometer observing a surface at a direction (θ,ϕ) is given, similarly to equation (1) in section 2.3, by the expression:

$$L_i(\theta,\phi) = \left(\varepsilon_i(\theta,\phi)B_i(T) + \left(1-\varepsilon_i(\theta,\phi)\right)L_i{}^{\downarrow}{}_{atm}(\theta,\phi\pm\pi)\right)\tau_i(\theta,\phi) + L_i{}^{\uparrow}{}_{atm}(\theta,\phi) \quad (8)$$

where $\tau_i(\theta,\phi)$ is the atmospheric transmittance and $L_i{}^{\uparrow}{}_{atm}(\theta,\phi)$ is the upwelling sky radiance required to atmospherically correct satellite-retrieved data. Equation (8) defines the radiance measured for each ENVISAT-AATSR view (nadir and forward) separately, and for the two TIR channels: band 6 centered at 10.857 μm (covering the same spectral range than our experimental measurements), and band 7 centered at 12.051 μm.

As equation (8) shows, the determination of surface temperature, *T*, from $L_i(\theta,\phi)$ requires $\varepsilon_i(\theta,\phi)$, and the determination of $\varepsilon_i(\theta,\phi)$ from $L_i(\theta,\phi)$ requires *T*. Therefore, the indeterminacy needs to be solved to analyze the emissivity difference between forward and nadir views.

One way is retrieving *T* previously and using equation (8) for each view as follows:

$$\varepsilon_{i,v} = \frac{A_{i,v}}{B_i(T) - L_{i,v}{}^{\downarrow}{}_{atm}} \quad (9)$$

where $A_{i,v} = \dfrac{L_{i,v} - L_{i,v}{}^{\uparrow}{}_{atm}}{\tau_{i,v}} - L_{i,v}{}^{\downarrow}{}_{atm}$ for each view, *v*, being *n* (nadir) or *f* (forward).

The temperature *T* was estimated by using the high-spatial-resolution EOS Terra-ASTER. EOS Terra-ASTER band 13 (centered at 10.657 μm) has been proved to be minimally affected by the atmosphere and has been used to estimate the true surface temperature (atmospherically and emissivity corrected) [30].

Extension to top of atmosphere of the crude oil emissivities experimentally measured was evaluated with ENVISAT-AATSR and EOS Terra-ASTER images over the BP Deepwater Horizon

oil slick. The oil spill took place in the Gulf of Mexico, off the Mississipi River Delta, at the end of April 2010, and was one of the largest accidental marine oil spills in the history of the petroleum industry [2]. We selected cloud-free and concurrent AATSR (ATS_TOA) and ASTER (AST_L1B) images over the oil slick on May 24th, 2010. Fig. 5 shows a false-color RGB (ASTER 3-2-1 bands, i.e., NIR-red-green, with 15m spatial resolution) and the TIR band 13 of the ASTER image (90m spatial resolution), together with vector layers selecting three study areas: the main body of the oil slick (OSmb, in red), a secondary area affected by the oil slick (OSsa, in yellow) and relatively near and practically clean seawater (SW, in light blue). The concurrent EOS Terra-MODIS MOD07 product was used to obtain the atmospheric temperature and water vapor profiles at 5km spatial resolution for the study areas. These profiles were introduced into the MODTRAN 5 atmospheric radiative transfer model (maritime aerosols were assumed) to simulate the atmospheric transmittances and sky radiances for each area, each image spectral band (ASTER 13 and AATSR 6), and each image viewing angle (8.6º for ASTER; 7.5º and 54.9º for AATSR nadir and forward views over the oil slick sample; and 4.1º and 55.1º for AATSR nadir and forward views over the seawater sample).

Table II shows the statistics for the surface temperatures T assessed by using the ASTER band 13 data for the study areas. The statistics include: minimum (min), maximum (max), mean ($\overline{T}$), standard deviation (σ), median (M_e), and robust standard deviation (σ_R, $\sigma_R(T)=M_e(|T-M_e(T)|)\cdot 1.4826$ [31]). M_e and σ_R minimize the influence of possible outliers and can be considered more consistent parameters than $\overline{T}$ and σ. The analysis of the T distributions for the study areas showed two different modes for the OSmb, which explains a higher σ_R for it than for the other areas. The bimodal distribution in the OSmb showed two temperature distributions centered in 301.6K and 302.4K, respectively, and with σ and σ_R lower than ±0.3K. The OSmb temperatures and the $M_e(T)$ values shown in Table II for OSsa and SW were used as T to retrieve nadir and forward ENVISAT-AATSR emissivities with equation (9).

Table III shows the statistics of the ENVISAT-AATSR band 6 (10.857 μm) nadir and forward emissivities, $\varepsilon_{6,n}$ and $\varepsilon_{6,f}$, obtained for the three areas with equation (9). This table also includes the 10.3-11.0 μm crude oil experimental data at 15º and 55º as reference values, ε_{ref}, for OS emissivity comparison. Niclòs et al. [25] proposed the following expression to obtain the ENVISAT-AATSR band 6 seawater emissivity for any observation angle, θ, and surface wind speed, U:

$$\varepsilon_6(\theta,U) = 0.99199\left[\cos(\theta^{(-0.037U+2.36)})\right]^{0.0343} \quad (10)$$

Table III includes SW reference values, ε_{ref}, from equation (10) for comparison. Negligible differences were obtained between $M_e(\varepsilon)$ and ε_{ref} for the three study areas (see line $M_e(\varepsilon)$ - ε_{ref} in Table III). Despite the fact that OSmb and OSsa areas probably have distinct quantities of oil on the surface and also oil thicknesses, similar emissivity values were obtained for both areas. An evident emissivity dependence on oil thickness was not observed, in agreement with the measurements in [3] and the laboratory emissivity data in [4] from 8 to 12 μm.

Alternatively, the same T can be assumed for both views over homogeneous surfaces and therefore equal $B_i(T)$ for each i band. In this case, emissivity at the forward-viewing angle, $\varepsilon_{i,f}$, is obtained from the nadir-view emissivity, $\varepsilon_{i,n}$, following the expression:

$$\varepsilon_{i,f} = \frac{A_{i,f}}{(A_{i,n}/\varepsilon_{i,n}) + (L_{i,n}{}^{\downarrow}{}_{atm} - L_{i,f}{}^{\downarrow}{}_{atm})} \quad (11)$$

Equation (11) was used to obtain forward emissivities from assumed nadir values for the study areas. The ENVISAT-AATSR band 6 nadir emissivity for the OS areas was considered as 0.957 from the experimental measurements, while a value of 0.992 was assumed for the SW area according to the model of Wu and Smith [27] and the experimental results of Niclòs et al. [25].

Table III also shows the statistics of the $\varepsilon_{6,f}$ obtained for the study areas with equation (11) from the assumed nadir emissivity values. Finally, differences between $M_e(\varepsilon)$ and ε_{ref} are included for comparison, showing again a good agreement for the three areas.

Therefore, there is a good agreement between experimental and satellite-retrieved emissivities, confirming that crude emissivity decrease with angle is larger than that for seawater emissivity.

5. SUMMARY AND CONCLUSIONS

Crude oil slicks cause an emissivity decrease relative to seawater in the TIR region. This paper characterizes crude oil and seawater emissivity spectral and angular variations. Crude oil emissivity measurements show a featureless grey-body spectrum within the 8 - 13 μm atmospheric window and a marked emissivity decrease with angle (from 0.956±0.005 at 15º to 0.873±0.007 at 65º). The paper also quantifies the emissivity difference between crude oil and seawater. Crude oil emissivity is lower than that of seawater, as previous papers have pointed out [3]-[4]. The seawater-crude emissivity differences have been quantified at different observation angles; the differences ranging from +0.030±0.007 at close-to-nadir angles to +0.068±0.010 in average at 65º.

The experimental conclusions were checked by using the dual-angle viewing capability of the ENVISAT-AASTR band 6 to explore the applicability to satellite TIR data. Emissivity differences between the BP Deepwater Horizon oil slick and surrounding clean seawater of -0.035 and -0.046 were shown for the nadir and forward views respectively, following the experimental results. Nadir-forward emissivity differences of +0.028 and +0.017 were obtained for the oil slick and seawater respectively, in agreement with the crude oil and seawater emissivity measurements and results of previous references about seawater emissivities [19], [24]-[27], [29].

Taking into account the seawater-crude emissivity difference results, crude oil slicks are identifiable from satellite TIR data. Crude oil emissivity decrease with angle is even larger than that for seawater, which makes crude oil slicks be more easily identifiable by comparing with seawater response from satellite TIR data at large observation angles.

6. AKNOWLEDGEMENTS

The research described in this paper was supported by the Spanish Ministerio de Ciencia e Innovación (projects CGL2010-16364, CGL2010-17577, CGL2011-13579-E, and CGL2011-30433; and Dr. Niclòs' "Ramón y Cajal" Research Contract) and the *Generalitat Valenciana* (PROMETEO/2009/086). The crude sample was provided by Repsol S.A. in the framework of a collaboration agreement between the University of Valencia and Repsol entitled "Characterization of physical-chemical and TIR-emissive properties". Finally, we would like to thank the reviewers for the thoughtful reviews of the manuscript, and for the valuable and detailed comments.

REFERENCES

[1] I. Leifer, W.J. Lehr, D. Simecek-Beatty, E. Bradley, R. Clark, P. Dennison, Y. Hu, S. Matheson, C.E. Jones, B. Holt, M. Reif, D.A. Roberts, J. Svejkovsky, G. Swayze, and J. Wozencraft, "State of the art satellite and airborne marine oil spill remote sensing: Application to the BP Deepwater Horizon oil spill," *Remote Sens. Environ.*, vol. 124, pp. 185–209, 2012.

[2] R.K. Perrons, "Assessing the damage caused by Deepwater Horizon: Not just another Exxon Valdez," *Mar. Pollut. Bull.,* vol. 71, pp. 20–22.

[3] J. W. Salisbury, D.M. D'Aria, and F. F. Sabins, "Thermal infrared remote sensing of crude oil slicks," *Remote Sens. Environ.*, vol. 45, pp. 225-231, 1993.

[4] T. Lammoglia, and C.R. De Souza Filho, "Spectroscopic characterization of oils yielded from Brazilian offshore basins: Potential applications of remote sensing," *Remote Sens. Environ.*, vol. 115, pp. 2525-2535, 2011.

[5] P. Camagni, G. Colombo, C. Koechler, A. Pedrini, N. Omenetto, and G. Rossi, "Diagnostics of oil pollution by laser-induced fluorescence," *IEEE Trans. Geosci. Remote Sens*., vol. 26, pp. 22-26, 1988.

[6] C. E. Brown, *Laser fluorosensors. Oil spill science and technology.* Boston: Gulf Professional Publishing, 2011, pp. 171–184.

[7] R. N. Clark, G. A. Swayze, I. Leifer, K.E. Livo, R. Kokaly, T. Hoefen, S. Lundeen, M. Eastwood, R.O. Green, N. Pearson, C. Sarture, I. McCubbin, D. Roberts, E. Bradley, D. Steele, T. Ryan, R. Dominguez, and the Air borne Visible/Infrared Imaging Spectrometer (AVIRIS) Team, *A method for quantitative mapping of thick oil spills using imaging spectroscopy*. Virginia: U.S. Geological Survey, 2010, Open-File Report 2010-1167, 51p.

[8] Z. Otremba, and J. Piskozub, "Modelling the bidirectional reflectance distribution function (BRDF) of seawater polluted by an oil film," *Opt. Express*, vol. 12, pp. 1671–1676, 2004.

[9] J. K. Buettner, and C.D. Kern, “The determination of infrared emissivities of terrestrial surfaces,” *J. Geophys. Res.*, vol. 70, pp. 1329-1337, 1965.

[10] S. Hashimoto, H. Nakano, and M. Yamaguchi, “Microwave radiometric detection and imaging of oil spills on the sea,” in *Proc. International Symposium on Remote Sensing of Environment Fourth Thematic Conf.*, San Francisco, California, Apr. 1-4, 1985, pp. 557-565.

[11] J. E. Estes, U.E. Crippen, and J.L. Star, “Natural oil seep detection in the Santa Barbara Channel, California, with Shuttle Imaging Radar,” *Geology,* vol. 13, pp. 282-284, 1985.

[12] B. Holt, “SAR imaging of the ocean surface,” in C. R. Jackson, & J. R. Apel (Eds.), *Synthetic aperture radar (SAR) marine user's manual*. Washington DC: NOAA NESDIS Office of Research and Applications, 2004, pp. 25–79.

[13] C. Brekke, and A.H.S. Solberg, “Oil spill detection by satellite remote sensing,” *Remote Sens. Environ.*, vol. 95, pp. 1–13, 2005.

[14] G. Brogniez, C. Pietras, M. Legrand, P. Dubuisson, and M. Haeffelin, “A high accuracy multiwavelength radiometer for in situ measurements in the thermal infrared. Part II: Behavior in field experiments,” *J. Atmos. Oceanic Technol.*, vol. 20(7), pp. 1023–1033, 2003.

[15] E. Theocharous, E. Usadi, and N. P. Fox. *NPL Report OP3*: *CEOS comparison of IR brightness temperature measurements in support of satellite validation. Part I: Laboratory and ocean surface temperature comparison of radiation thermometers,* Teddington, UK: National Physical Laboratory (NPL), 2010.

[16] F. E Nicodemus, “Directional reflectance and emissivity of an opaque surface,” *Appl. Opti*cs, vol. 4, pp. 767-773, 1965.

[17] F. E. Nicodemus, J.C. Richmond, J.J. Hsia, I.W. Ginsberg, and T. Limperis, *Geometrical considerations and nomenclature for reflectance*, Washington, DC: National Bureau of Standards, US Department of Commerce, 1977.

[18] I. J. Barton, A.M. Zavody, D.M. O'Brien, D.R. Cutten, R.W. Saunders, and D.T. Llewelling-Jones, "Theoretical algorithms for satellite derived sea surface temperatures," *J. Geophys. Res.*, vol. 94, pp. 3365– 3375, 1989.

[19] R. Niclòs, E. Valor, V. Caselles, C. Coll, and J.M. Sánchez, "In situ angular measurements of thermal infrared sea surface emissivity - Validation of models," *Remote Sens. Environ.*, vol. 94(1), pp. 83-93, 2005.

[20] V. García-Santos, E. Valor, V. Caselles, M. Mira, J.M. Galve, and C. Coll, "Evaluation of Different Methods to Retrieve the Hemispherical Downwelling Irradiance in the Thermal Infrared Region for Field Measurements," *IEEE Trans. Geosci. Remote Sens.*, vol. 99, pp. 1-11, 2012.

[21] E. Rubio, V. Caselles, and C. Badenas, "Emissivity measurements of several soils and vegetation types in the 8–14 μm waveband: Analysis of two field methods," *Remote Sens. Environ.*, vol. 59(3), pp. 490–521, 1997.

[22] R. Niclòs, V. Caselles, C. Coll, E. Valor, and J.M. Sánchez, "In situ surface temperature retrieval in a boreal forest under variable cloudiness conditions," *Int. J. Remote Sens.*, vol. 26 (18), pp. 3985-4000, 2005.

[23] J. W. Salisbury, and D.M. D'Aria, "Emissivity of terrestrial materials in the 8-14 μm atmospheric window," *Remote Sens. Environ*., vol. 42, pp. 83-106, 1992.

[24] R. Niclòs, V. Caselles, E. Valor, and C. Coll, "Foam effect on the sea surface emissivity in the 8-14 μm region," *J. Geophys. Res.*, vol. 112, C12020, 2007.

[25] R. Niclòs, V. Caselles, E. Valor, C. Coll, and J.M. Sanchez, "A simple equation for determining the sea surface emissivity in the 3-15μm region," *Int. J. Remote Sens.*, vol. 30 (6), pp. 1603–1619, 2009.

[26] W. L. Smith, R.O. Knuteson, H. E. Revercomb, W. Feltz, H. B. Howell, W. P. Menzel, et al., "Observations of the infrared radiative properties of the ocean—implications for the measurement

of sea surface temperature via satellite remote sensing*," B. Am. Meteorol. Soc.*, vol. 77, pp. 41–51, 1996.

[27] X. Wu, and W. L. Smith, "Emissivity of rough sea surface for 8–13 μm: modelling and verification," *Appl. Optics*, vol. 36, pp. 2609– 2619, 1997.

[28] H. Li, N. Pinel, and C. Bourlier, "Polarized infrared emissivity of one-dimensional Gaussian sea surfaces with surface reflections," *Appl. Optics*, vol. 50, pp. 4611 – 4621, 2011.

[29] H. Li, N. Pinel, C. Bourlier, "Polarized infrared emissivity of 2D sea surfaces with one surface reflection," *Remote Sens. Environ.*, vol. 124, pp. 299–309, 2012.

[30] C. Coll, V. Caselles, E. Valor, R. Niclòs, J.M. Sánchez, J.M. Galve, and M. Mira, "Temperature and emissivity separation from ASTER data for low spectral contrast surfaces," *Remote Sens. Environ.*, vol. 110, pp. 162–175, 2007.

[31] P. T. Wilrich, "Robust estimates of the theoretical standard deviation to be used in interlaboratory precision experiments," *Accredit. Qual. Assur.*, vol. 12, 231–240, 2007.

TABLES

Table I.- Properties of the crude sample

°API		33.0
SARA fractionation % m/m (by mass)	saturated hydrocarbons	64
	aromatic hydrocarbons	18
	resins	11
	C5 asphaltenes	6
	Sulfur	0.3
viscosity (m^2s^{-1}) at 20ºC		$19.0 \cdot 10^{-6}$
viscosity (m^2s^{-1}) at 40ºC		$6.5 \cdot 10^{-6}$
Watson k-factor		12

Table II.- Surface temperature statistics for the three samples: seawater (SW), the main body of the oil slick (OSmb) and the secondary area affected by the oil slick (OSsa) (EOS Terra-ASTER 05/24/2010)

T (K)	SW	OSmb	OSsa
min(T)	298.79	300.3	300.9
max(T)	300.32	304.6	304.1
$\overline{T}$	299.59	302.0	302.5
$\sigma(T)$	0.17	0.5	0.4
$M_e(T)$	299.61	302.0	302.5
$\sigma_R(T)$	0.16	0.6	0.4

Table III.- ENVISAT-AATSR band 6 nadir emissivity obtained with equation (9) and forward emissivities obtained with equations (9) and (11) for seawater (SW) and oil slick samples (main body, OSmb, and secondary area, OSsa). Oil slick ε_{ref} values were taken from the crude oil emissivity measurements and SW ε_{ref} values were calculated with equation (10).

	SW			OSmb			OSsa		
	$\varepsilon_{6,n}$	$\varepsilon_{6,f\,eq.(9)}$	$\varepsilon_{6,f\,eq.(11)}$	$\varepsilon_{6,n}$	$\varepsilon_{6,f\,eq.(9)}$	$\varepsilon_{6,f\,eq.(11)}$	$\varepsilon_{6,n}$	$\varepsilon_{6,f\,eq.(9)}$	$\varepsilon_{6,f\,eq.(11)}$
min(ε)	0.985	0.968	0.966	0.938	0.897	0.899	0.940	0.915	0.910
max(ε)	0.999	0.985	0.984	0.982	0.962	0.960	0.971	0.964	0.977
$\bar{\varepsilon}$	0.993	0.976	0.975	0.959	0.933	0.930	0.956	0.933	0.934
σ(ε)	$2.4\cdot10^{-3}$	$3.8\cdot10^{-3}$	$3.5\cdot10^{-3}$	$6.0\cdot10^{-3}$	$11.2\cdot10^{-3}$	$9.8\cdot10^{-3}$	$6.0\cdot10^{-3}$	$13.0\cdot10^{-3}$	$12.0\cdot10^{-3}$
$M_e(\varepsilon)$	0.993	0.976	0.975	0.959	0.931	0.930	0.957	0.929	0.932
$\sigma_R(\varepsilon)$	$2.6\cdot10^{-3}$	$3.8\cdot10^{-3}$	$3.6\cdot10^{-3}$	$5.3\cdot10^{-3}$	$10.5\cdot10^{-3}$	$10.6\cdot10^{-3}$	$5.6\cdot10^{-3}$	$11.5\cdot10^{-3}$	$11.3\cdot10^{-3}$
ε_{ref}	0.992	0.975	0.975	0.957	0.929	0.929	0.957	0.929	0.929
$M_e(\varepsilon)$ - ε_{ref}	$8.7\cdot10^{-4}$	$7.8\cdot10^{-4}$	$3.4\cdot10^{-4}$	$1.7\cdot10^{-3}$	$1.7\cdot10^{-3}$	$7.0\cdot10^{-4}$	$-2.6\cdot10^{-4}$	$-1.5\cdot10^{-4}$	$2.5\cdot10^{-3}$

FIGURE CAPTIONS

Fig. 1.- Fit of sky radiance measurements taken by the CE312 8-13μm spectral band to the cloud-free relationship given by equation (7), where x_i is given by the fitting slope value (x_i=0.4951). The dispersions of the sky radiance measurements taken at each angle led to y-axis uncertainties lower than ±0.002; invisible in the figure.

Fig. 2.- Spectral signatures of the crude oil and seawater emissivities measured at the close-to-nadir angle of 15º, together with seawater emissivity measurements previously published in [19] and [23].

Fig. 3.- Spectral signatures of the crude oil and seawater emissivities measured at observation angles of 15º and 65º.

Fig. 4.- Angular variation of seawater and crude oil emissivities, and the difference between them.

Fig. 5.- EOS Terra-ASTER false-color image (3-2-1 RGB bands) and TIR band 13 (at 15m and 90m spatial resolutions respectively), together with three vector layers selecting the study areas: the main body of the oil slick (OSmb, in red), a secondary area affected by the oil slick (OSsa, in yellow) and relatively near and practically clean seawater (SW, in light blue).

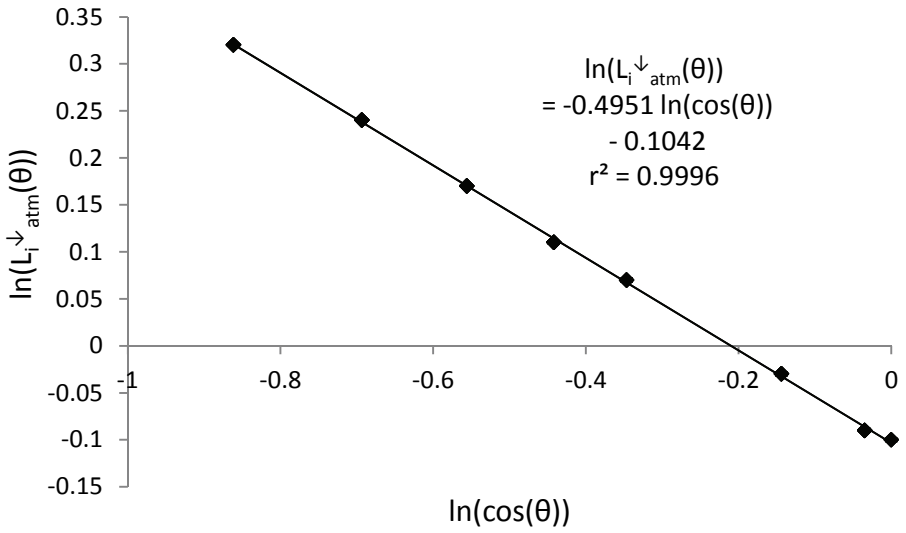
0.35
0.3
0.25
0.2
0.15
0.1
0.05
0
-0.05
-0.1
-0.15
-1
-0.8
-0.6
-0.4
-0.2
0
ln(L↓atm(θ))
ln(cos(θ))
ln(L↓atm(θ))
= -0.4951 ln(cos(θ))
- 0.1042
r² = 0.9996

Fig. 1

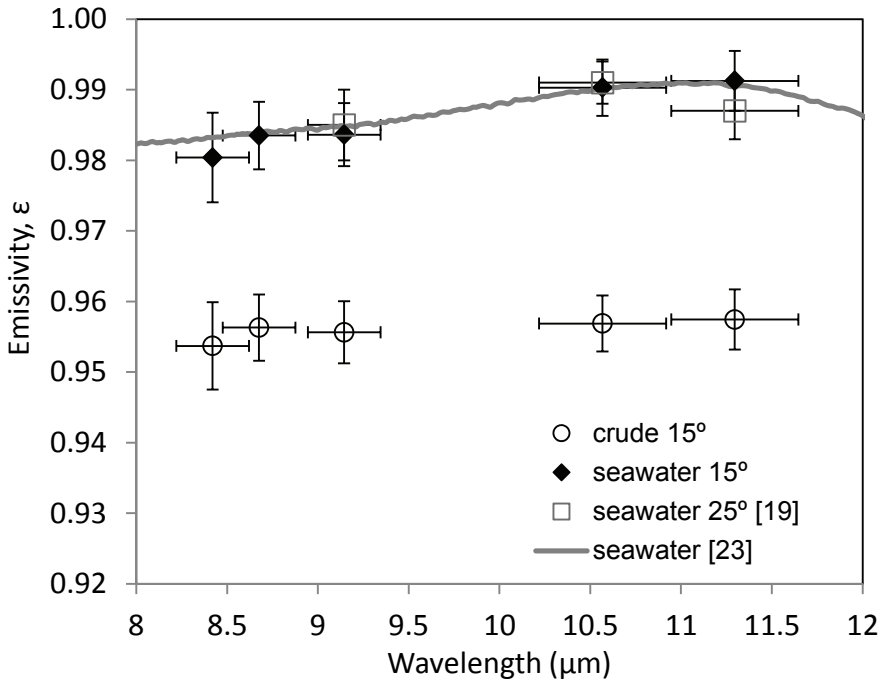
1.00
0.99
0.98
0.97
0.96
0.95
0.94
0.93
0.92
Emissivity, ε
8
8.5
9
9.5
10
10.5
11
11.5
12
Wavelength (μm)
crude 15°
seawater 15°
seawater 25° [19]
seawater [23]

Fig. 2

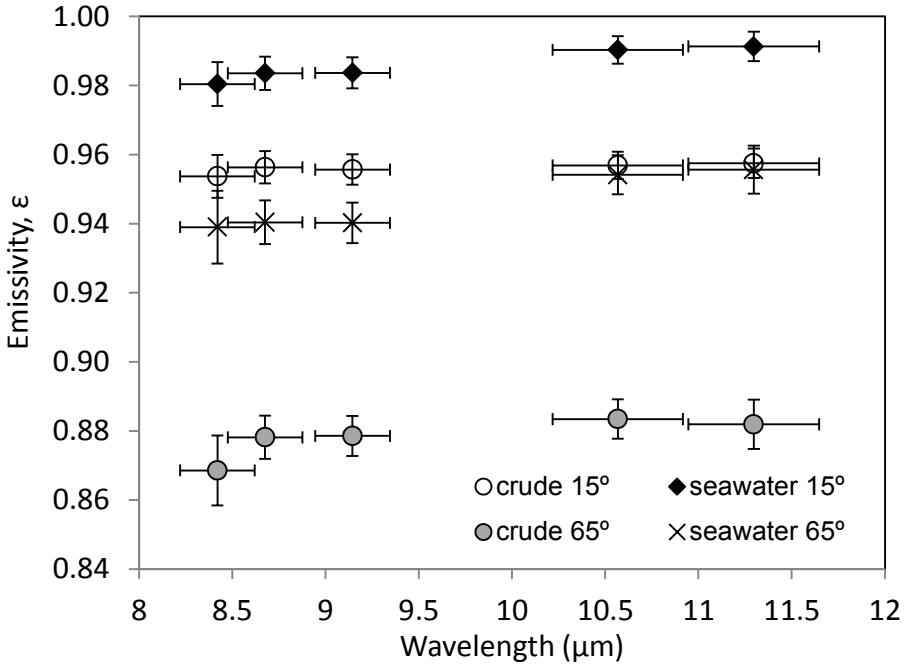
1.00
0.98
0.96
0.94
0.92
0.90
0.88
0.86
0.84
Emissivity, ε
8
8.5
9
9.5
10
10.5
11
11.5
12
Wavelength (μm)
crude 15º
seawater 15º
crude 65º
seawater 65º

Fig. 3

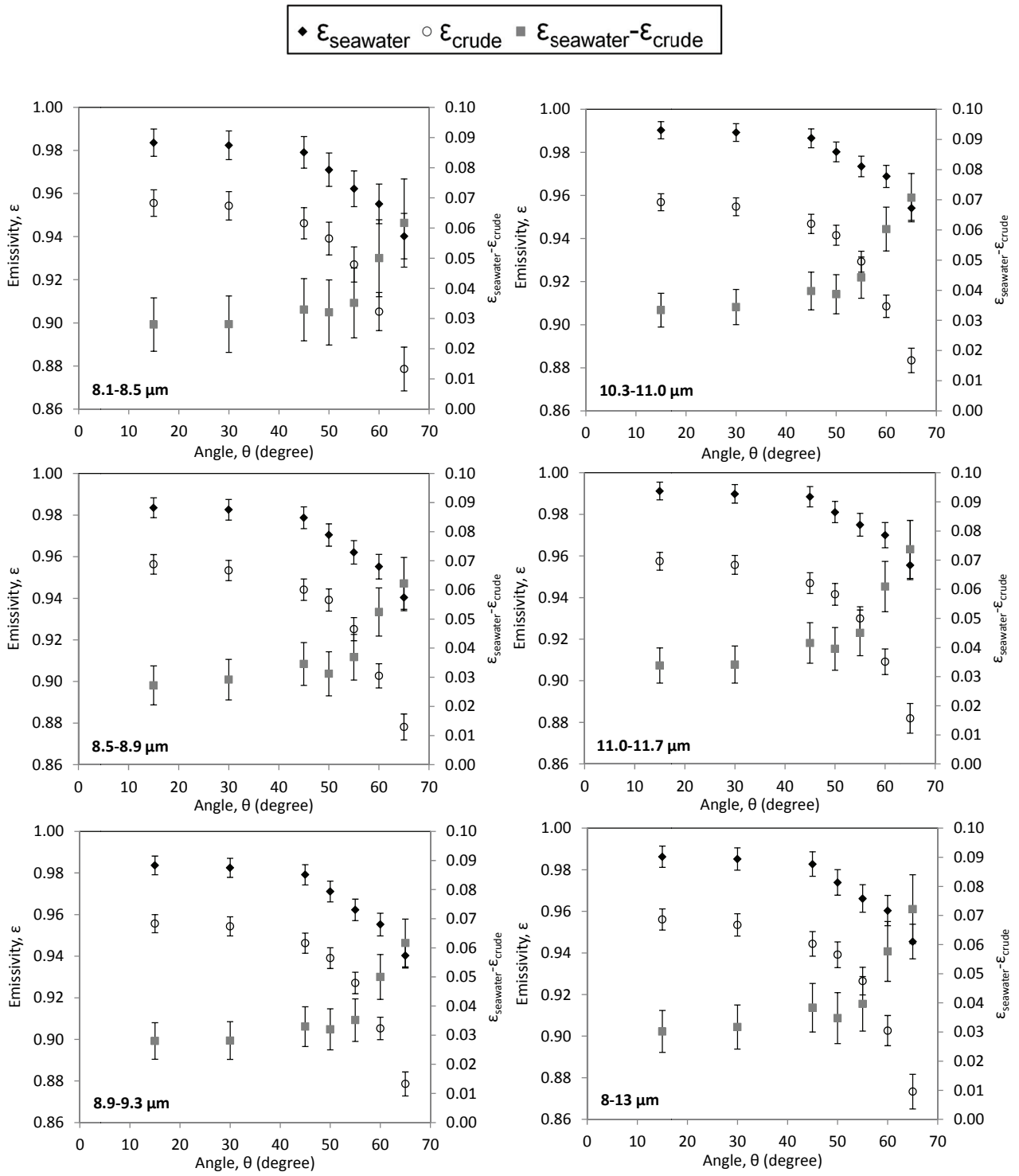
ε seawater ε crude ε seawater-ε crude
Emissivity, ε
ε seawater-ε crude
Angle, θ (degree)
8.1-8.5 µm
10.3-11.0 µm
8.5-8.9 µm
11.0-11.7 µm
8.9-9.3 µm
8-13 µm

Fig. 4

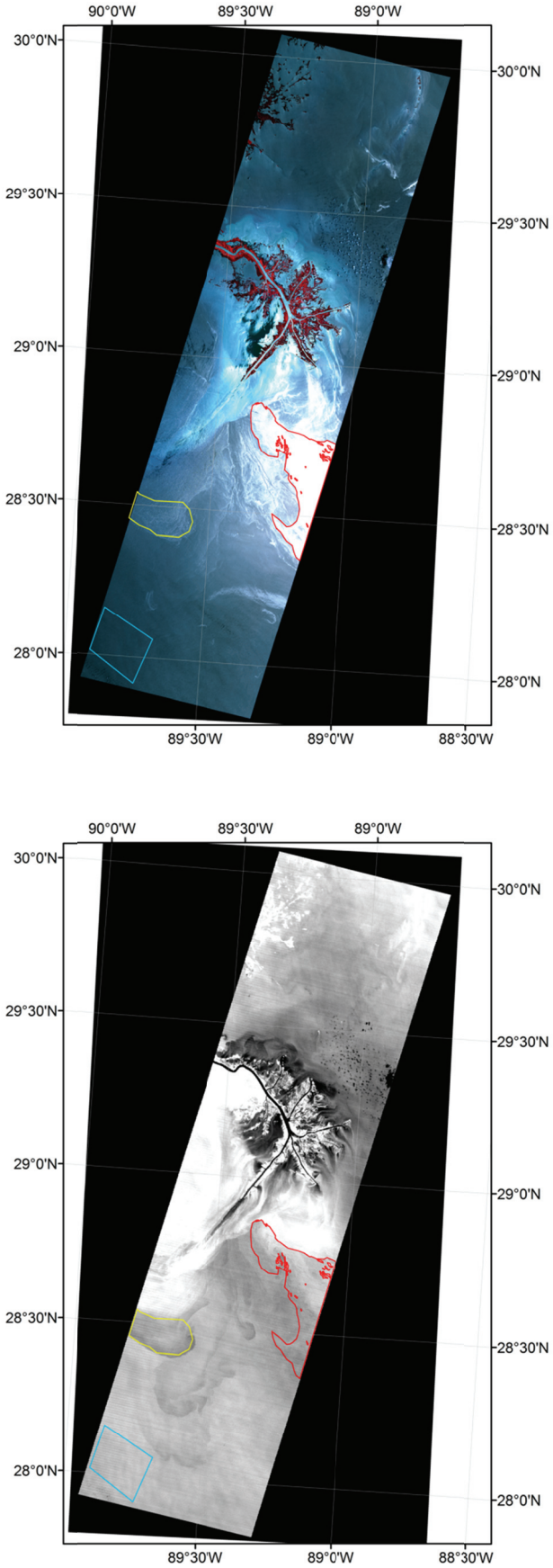

Fig. 5